Available online at www.sciencedirect.com
ScienceDirect
Trans. Nonferrous Met. Soc. China 32(2022) 1805−1821

Transactions of Nonferrous Metals Society of China
www.tnmsc.cn

Quantitative analysis of influence of α-Al(MnFeCr)Si dispersoids on hot deformation and microstructural evolution of Al−Mg−Si alloys

Hiromi NAGAUMI[1,2], Jian QIN[1,2], Cheng-bin YU[1,2], Xiao-guo WANG[1,3], Lin-sheng WANG[4]

1. High Performance Metal Structural Materials Research Institute, Soochow University, Suzhou 215021, China;
2. Shagang School of Iron and Steel, Soochow University, Suzhou 215021, China;
3. College of Agricultural Engineering, Shanxi Agricultural University, Taigu 030801, China;
4. Press Metal International Ltd., Foshan 528000, China

Received 5 June 2021; accepted 18 December 2021

Abstract: The microstructural evolution of AA6061 and Mn-bearing Al−Mg−Si−Cu alloys was studied by compression tests that were carried out between 300 and 500 °C with a wide range of strain rates. Compared to the AA6061 alloy, the large amount of α-Al(MnFeCr)Si dispersoids in the Mn-bearing alloy yielded a significant increase in the flow stress under all deformation conditions. The effects of the deformation parameters on the evolution of the microstructure were studied using electronic backscatter diffraction measurements. The predominant softening mechanism of both alloys was dynamic recovery. The presence of α dispersoids in Mn-bearing alloys effectively refined the size of substructures with misorientation angles in the range of 2°−5°, which retarded the dynamic recovery. To predict the subgrain size under various deformation conditions, the threshold stresses that were caused by α dispersoids were calculated by the modified Orowan equation and incorporated into a conventional constitutive equation. The subgrain size that was predicted by the modified constitutive equation showed satisfactory agreement with the experimental measurements.

Key words: Al−Mg−Si alloy; hot deformation; α-Al(MnFeCr)Si dispersoids; substructure; dynamic softening; threshold stress; Z parameter

1 Introduction

Al−Mg−Si−Cu 6xxx alloys have been widely applied in the automotive industry owing to their excellent formability, mass reduction, and mechanical properties [1−3]. Thermomechanical processing, such as extrusion, rolling, or forging, is an important step in the fabrication of wrought Al alloy products with excellent mechanical properties. With the rapid development of electric vehicles, high-strength, high-toughness and high-fatigue resistance aluminum alloys are more in demand than ever before. Substructures have been reported to retard the propagation of fatigue cracks [4] and promote dynamic precipitation, which enhances the strength of various alloys [5]. Due to the high stacking-fault energy of Al alloys, dynamic recovery (DRV) is the preferentially initiated softening mechanism during high-temperature deformation, which results in the formation of abundant substructures [6,7]. Therefore, the introduction of high-density substructures into internal grains is a promising approach for improving Al alloy fatigue and mechanical properties. With the addition of transition elements, such as Mn, Cr, and/or Mo, partially coherent nanoscale α-Al(Mn,Fe)Si dispersoids will precipitate in 3xxx and 6xxx alloys via the application of homogenization heat treatments [3,8]. These dispersoids can not only improve the alloy strength at both room and elevated temperatures but

---

Corresponding author: Jian QIN, Tel: +86-16623040289, E-mail: jian.qin@uqac.ca
DOI: 10.1016/S1003-6326(22)65910-7

also significantly improve the alloy recrystallization resistance [2,3] by inhibiting substructure migration. Therefore, the development of dispersoid-strengthened Al alloys is of great interest for both academic studies and industrial applications [2,8].

According to GUEMINI et al [9], AlFeSi dispersoids can increase the recrystallization temperature. TROEGER and STARKE [10] suggested that α-Al(Mn,Fe)Si dispersoids in Al alloys are important for fine and homogeneous grain structures. KENYON et al [11] demonstrated that the pinning effectiveness of dispersoids against recrystallization is sensitive to their fraction, size, and morphology. HU et al [12] showed that the morphology of α-Al(Mn,Fe)Si dispersoids substantially influences the recrystallization and grain growth behaviors of Al−Mg−Si−Mn alloys. STROBEL et al [13] and POLETTI [14] reported that dispersoids can improve recrystallization resistance, which is ascribed to the Zener drag force on grain boundary migration. However, research that examines the impact of dispersoids on the flow stress behavior and the microstructural evolution of Al−Mg−Si alloys during hot deformation has rarely been reported. The influence of α-Al(MnFeCr)Si dispersoids on the subgrain growth mechanism has been studied even less. QIAN et al [15] showed that the precipitation of dispersoids facilitates the retardation of DRV and the inhibition of the dynamic recrystallization (DRX), and is attributed to the pinning effect of dispersoids on dislocation movement and subgrain boundary migration. However, the mechanism by which α-Al(MnFeCr)Si dispersoids retard DRV and DRX and influence hot deformation remains unclear. The relationship between α-Al(MnFeCr)Si dispersoids and substructure size needs to be clarified. According to the research of GÜZEL et al [16], there are two kinds of Al alloy DRX: continuous dynamic recrystallization (cDRX) and geometric dynamic recrystallization (gDRX). It is well accepted that cDRX accompanies dislocation accumulation and transformation of low-angle boundaries (LABs) to high-angle boundaries (HABs) by extensive subgrain rotation [17]. gDRX is often observed when alloys are deformed and undergo large strains. McQUEEN and IMBERT [18] and POLETTI et al [14] observed gDRX in hot deformed 1xxx and 6082 alloys, respectively. Hence, further investigation and quantitative analysis of the influence of α dispersoids on hot processing must be conducted.

In the present work, a new type of Al−Mg−Si−Cu alloy with the addition of 0.5 wt.% Mn (named WQ1) and the 6061 alloy were systematically compared in terms of hot deformation and microstructural evolution as functions of the deformation temperature, strain and strain rate. The microstructural evolution of both alloys was characterized and quantified to examine the dynamic softening mechanisms and the mechanisms via which α dispersoids restrain DRV and DRX. A combination of Orowan strengthening theory and the hyperbolic sine constitutive equation was used to predict the subgrain size according to the volume fractions, α-Al(MnFeCr)Si dispersoid sizes, and deformation conditions.

2 Experimental

The alloys used in this work were 6061 and WQ1 Al alloys that were manufactured by direct chill casting. Ingots of 6061 and WQ1 with diameters and heights of 150 mm and 100 mm, respectively, were homogenized. The 6061 alloy was heat-treated at 555 °C for 6 h with a heating rate of 111 °C/h. To avoid coarsening of the α dispersoids, the WQ1 alloy was homogenized at 530 °C for 6 h with a heating rate of 133 °C/h. To prevent the dispersoids in the WQ1 alloy from being overcoarsened, the homogenization heat treatment temperature was lower than that for 6061. After homogenization heat treatment, the ingots of both alloys were air-cooled to ambient temperature. The chemical compositions of these two alloys were examined by optical emission spectroscopy with Spectrolab equipment, and the results are listed in Table 1. Cylindrical hot compression samples of 10 mm in diameter and 15 mm in height were machined from the half-radius to the center of the homogenized ingots. To observe the distribution of α dispersoids in the alloys, the samples were etched in 0.5 vol.% HF solution for 20 s at ambient

Table 1 Chemical compositions of WQ1 and 6061 Al alloys (wt.%)

Alloy	Mg	Si	Cu	Mn	Cr	Fe	Ti	Al
WQ1	0.9	1.0	0.45	0.48	0.3	0.12	0.02	Bal.
6061	1.06	0.68	0.25	0.02	0.17	0.16	0.03	Bal.

temperature. The samples were anode-coated at 18 V in a solution of 38 vol.% H_2SO_4 + 43 vol.% HNO_3 + 19 vol.% deionized water for 1.5 min to determine the average grain size.

A Gleeble−3500 thermomechanical simulator was employed to carry out the isothermal compression deformation experiments over a deformation temperature range from 300 to 500 °C with a strain rate from 0.01 to 10 s^{-1} to a true strain of 1.2. Graphite foils were placed on both sides of each sample for lubrication. Thermocouples were inserted in every sample to precisely control the deformation temperature, and the samples were heated to the targeted temperature at a heating rate of 5 °C/s and subsequently soaked for 2 min to remove the thermal gradients.

The samples were immediately quenched into water at ambient temperature after hot deformation to preserve the compressed microstructures. Cross-sections of the specimens were obtained from the central part of the deformed samples for microstructural characterization, parallel to the compression direction, and subsequently mounted, ground, polished, and electropolished in 10 vol.% perchloric acid + 90 vol.% ethanol to produce strain-free surfaces for electron backscattering diffraction (EBSD) analysis. EBSD mapping was only performed in central areas of the compressed samples with step sizes of 1 μm and 0.3 μm, and the corresponding scan areas were 600 μm × 480 μm and 150 μm × 120 μm, respectively. The index ratio of EBSD mapping ranged from 76% to 92%, which depended on the deformation temperature. High-angle boundaries (HABs) are defined as misorientations that are larger than 15°, while LABs are defined as misorientations that are between 2° and 15°. Boundaries with misorientation angles of less than 2° were not considered. To distinguish LABs from HABs in the EBSD IPF images, all the LABs are shown as white lines, while all the HABs are shown as black lines. The microstructural evolution was observed using a JEOL JEM−2100F field emission transmission electron microscope (TEM) that was operated at 200 kV. The TEM samples were prepared by the twin-jet electropolishing method at −20 °C using a 75 vol.% methanol and 25 vol.% HNO_3 solution. Convergent beam electron diffraction (CBED) patterns were used to measure the thickness of the TEM specimens. The precipitate volume fractions and equivalent diameters were determined via TEM image analysis. To consider the precipitate truncation effect in the TEM images, the method in Ref. [19] was used to calculate the volume fraction.

3 Results and discussion

3.1 Initial microstructure

The microstructures of the homogenized 6061 and WQ1 alloys are shown in Fig. 1, and their grain sizes are (95.75±6.34) and (216.76±13) μm, respectively. During homogenization heat treatment, the needle-like β-Al_5FeSi phases transformed into rounded α-AlFeMnSi intermetallic phases, and the coarse primary Mg_2Si phases dissolved into the Al matrix [20,21]. Mn was introduced into 6xxx Al alloys because it could promote transformation from the β iron-bearing phase to the α iron-bearing phase. According to the energy dispersive spectroscopy (EDS) results, which are shown in Figs. 1(g, h), the intermetallic phases in the 6061 alloy consisted mainly of spheroidizing primary Mg_2Si and α-Al(FeMnCr)Si. Rod-like Mg_2Si phases that precipitated during cooling after the homogenization process are also observed in Fig. 1(c). In the WQ1 alloy, spheroidized primary Mg_2Si and α-Al(MnFeCr)Si are also observed and are marked in Fig. 1(d). During direct chill casting, some Fe and Mn elements were constrained in the matrix of the Al; these elements precipitated in the form of α-Al(MnFeCr)Si dispersoids during subsequent heat treatments. To distinguish the distribution of the α dispersoids, samples of 6061 and WQ1 alloys were etched by 0.5% HF, and their microstructures are shown in Figs. 1(e, f), respectively. According to previous work [22], the gray areas in Figs. 1(e, f) represent the distribution of α dispersoids. Figure 1(f) includes a large and dense gray area, which indicates that a large amount of α dispersoids precipitated in the interior of the WQ1 alloy grains during homogenization heat treatment, while in Fig. 1(e), few α-Al(MnFeCr)Si dispersoids are observed in the grains of the 6061 alloy due to a lack of essential Mn (Table 1) and a large area of dispersoid-free zones (DFZs). Moreover, DFZs were present at the grain boundaries and in interdendrite arm areas, as shown in Fig. 1(f).

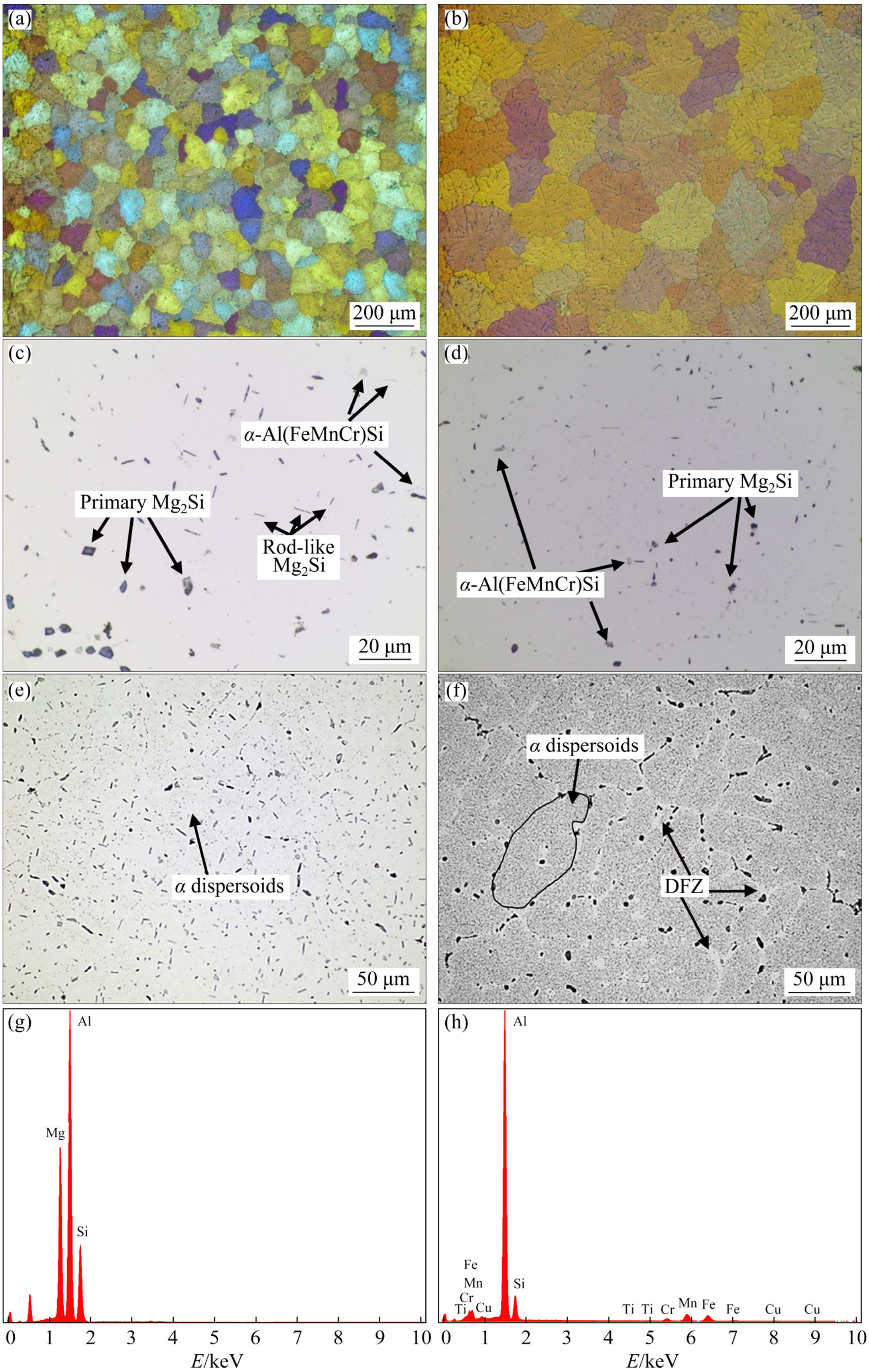

Fig. 1 Optical microscopy images of 6061 (a, c, e) and WQ1 (b, d, f) alloys under homogenization conditions, and EDS results of Mg_2Si (g) and α-Al(MnFeCr)Si dispersoids (h)

TEM was applied to characterizing the α dispersoids in the 6061 and WQ1 alloys under homogenization conditions, and the corresponding TEM images are shown in Figs. 2(a) and (b), respectively. Based on a quantitative TEM image analysis of the α dispersoids in both alloys, the average equivalent diameters were determined to be (364±75) and (129±33) nm for the 6061 and WQ1 alloys, respectively. The 6061 alloy contained not only fewer but also much coarser *α* dispersoids than the WQ1 alloy, which resulted in different hot deformation and microstructural evolution trends.

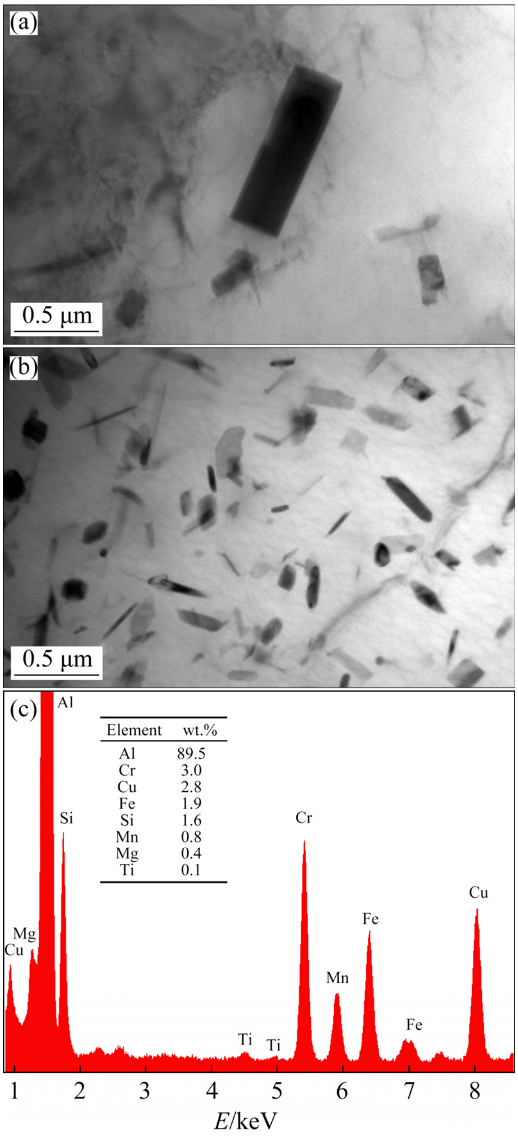

Fig. 2 TEM images of *α*-Al(MnFeCr)Si dispersoids in homogenized 6061 (a) and WQ1 (b) alloys and EDS result for *α*-Al(MnFeCr)Si dispersoids (c)

3.2 Flow stress behavior

It is concluded from Fig. 3 that the flow behaviors of both the WQ1 and 6061 Al alloys exhibited the same two-stage tendency, namely, rapid work hardening at the beginning stage of deformation and then a dynamic balance between dynamic softening and work hardening. As is well understood [23−25], work hardening phenomenon results from dislocation generation and propagation, while dynamic softening mechanisms are normally attributed to DRV [26,27] and DRX [28,29]. DRX is always accompanied by a reduction in flow stress; hence, DRX is not an operational mechanism for either alloy. It was clear that at the same strain rate and deformation temperature, the WQ1 alloy, with a higher solute atom content and more massive nanoscale *α*-Al(MnFeCr)Si dispersoids, which acted as obstacles to dislocation movement, exhibited higher flow stress than the 6061 alloy. The influence of *α*-Al(MnFeCr)Si dispersoids on the flow stress further affected the constitutive analysis of the WQ1 alloy. In our previous work, the average activation energy (*Q*) was calculated for both the 6061 alloy and WQ1 alloy, and the resulting values were 148.7 and 189.1 kJ/mol, respectively [30]. Compared to the 6061 alloy, the WQ1 alloy, which contained a large amount of *α*-Al(MnCr)Si dispersoids, also underwent a different microstructural evolution during hot deformation.

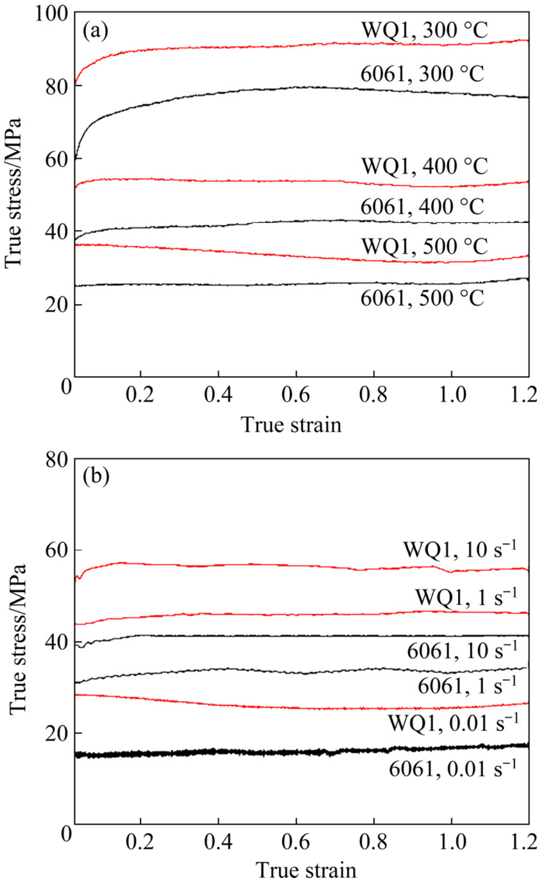

Fig. 3 Typical true stress–true strain plots of 6061 and WQ1 at strain rate of 0.1 s^{-1} and various deformation temperatures (a), and at 500 °C and different strain rates (b)

3.3 Microstructural evolution

The EBSD technology was employed to characterize the evolution of the alloy microstructure during hot deformation under various conditions. To examine the effect of strain on the microstructural evolution, the 6061 and WQ1 alloys were compressed to various strains at 300 °C with a strain rate of 0.1 s^{-1}. Figures 4 (a, b, c) show typical inverse pole figures (IPFs) of EBSD measurements of the 6061 alloy after deformation under the conditions that are specified above to strains of 0.5, 0.8 and 1.2, respectively. To further study the evolution of the substructure, EBSD measurements at higher magnification were characterized in the center zones of Figs. 4(a, b, c), which are marked by red frames, as shown in Figs. 4(d, e, f), respectively. Meanwhile, the IPF map is shown in Fig. 4(g), and all the EBSD measurements in the present work were collected by scanning along the same direction, which was perpendicular to the compression direction (CD). With increasing strain from 0.5 to 0.8, the microstructures of the 6061 alloy transformed from the original equiaxed grains to elongated grains, and the grain boundaries were serrated, as shown in Figs. 4(a, b). Up to a strain of 1.2, many fine and equiaxed recrystallized grains were observed at the original grain boundaries (Fig. 4(c)). Figures 4(d, e, f) show that the substructures of the 6061 alloy fully developed and were distributed in the interior of the original grains. The substructure size became finer and progressively associated with increasing strain, thereby indicating that the operational softening mechanism was DRV. As all the EBSD maps are IPF images, the difference in color between subgrains represents the misorientation between them [31]. There were large areas of substructures in the 6061 alloy with obviously different orientations, and this phenomenon intensified with increasing strain. Meanwhile, the substructure boundaries migrated through subgrain rotation, which promoted the transition of LABs to HABs, as marked with the red and yellow circles in Figs. 4(d, e, f). The newly formed HABs were combined together and elongated with increasing strain. At a strain of 1.2, recrystallized grains were formed, which are marked by black frames in Fig. 4(f), thereby indicating the occurrence of cDRX.

Similar to the 6061 alloy, in the WQ1 alloy (Fig. 5), DRV was the main softening mechanism until a strain of 1.2 (Fig. 5(c)). In addition, the misorientation between substructures in the WQ1 alloy was not as intense as that in the 6061 alloy. The transformation of substructure boundaries from LABs to HABs was limited until a strain of 0.8 (Fig. 5(e)). In Figs. 5(c, f), several original grains underwent recrystallization, while others maintained a DRV microstructure. The reason for this abnormal phenomenon is not clear and should

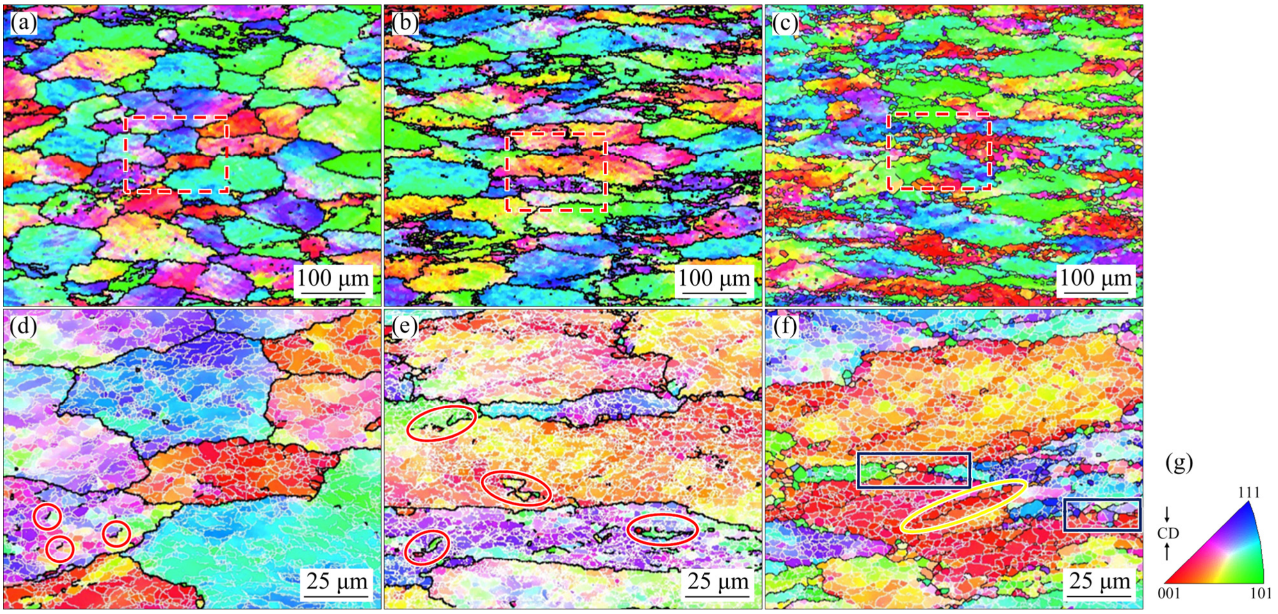

Fig. 4 EBSD IPF images of 6061 alloy after deformation at 300 °C and strain rate of 0.1 s^{-1} to strains of 0.5 (a, d), 0.8 (b, e) and 1.2 (c, f) and inverse pole figure with compression direction (CD) (g)

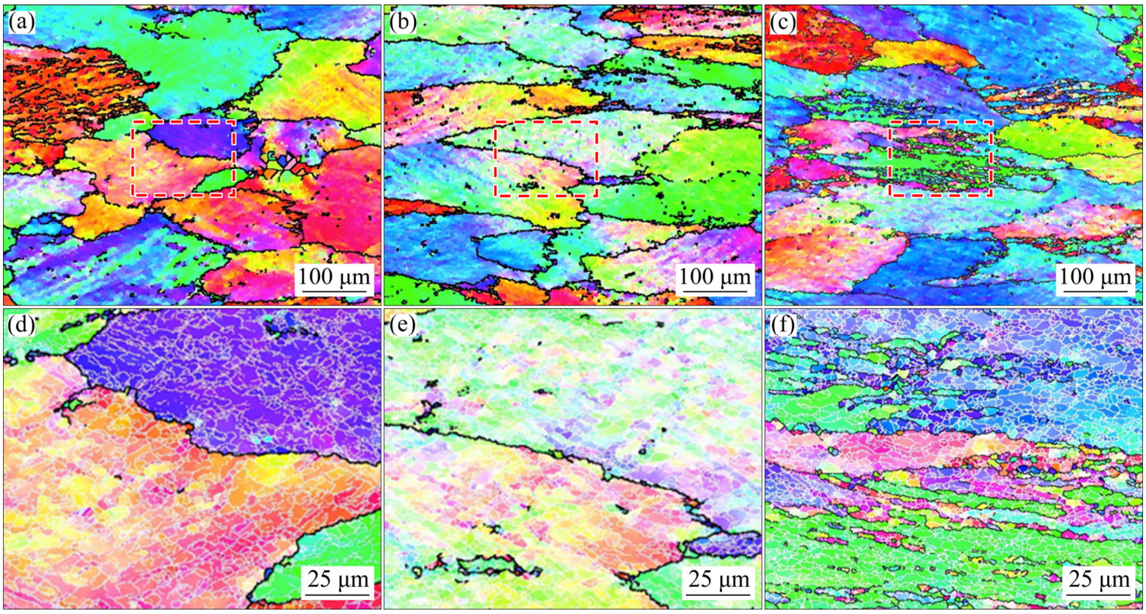

Fig. 5 EBSD IPF images of WQ1 alloy after deformation at 300 °C with strain rate of 0.1 s^{-1} to strains of 0.5 (a, d), 0.8 (b, e) and 1.2 (c, f)

be related to the lack of alloying elements, as reported in our previous work [32].

Based on the data from Figs. 4 and 5, Fig. 6 shows the evolution of the subgrain sizes in the 6061 and WQ1 alloys as functions of the strain. In both alloys, the subgrain sizes were almost the same and independent of the strain, indicating that a balance reached between DRV and work hardening. Limited by the low deformation temperature, subgrain boundary migration was restricted. Hence, the subgrain sizes of both alloys were almost constant and nearly the same.

The DRV levels varied with the deformation conditions, which is demonstrated by the misorientation angle distribution. To further examine the effect of *α* dispersoids on the deformation substructure, the misorientation angle distribution of the substructures was subdivided into two regions, namely, 2°−5° and 5°−15°, and HABs for which the misorientation was ≥15° were also considered. Based on the mapping data of Figs. 4 and 5, the relative frequencies of the subgrains and grains in these three misorientation regions as functions of the strain are illustrated in Fig. 7. Among the three regions, for both alloys, the higher frequency of the LABs in the deformed microstructure was concentrated mainly in the substructure region in which the misorientation was 2°−5°, which also suggested that the main operative mechanism was DRV. Additionally, for both alloys, in the region of LABs (2°−5°), the relative frequencies of the subgrains decreased slightly with increasing strain. Moreover, the WQ1 alloy always had a higher frequency than the 6061 alloy in this region. In the other two misorientation regions, the frequencies of both alloys mainly increased with increasing strain. In addition, the frequency of the 6061 alloy was always greater than that of the WQ1 alloy in the other three misorientation regions. Under the influence of *α* dispersoids, substructure rotation in the WQ1 alloy was not readily observed at a strain of 0.5 (Fig. 5(d)). Only partial rotation

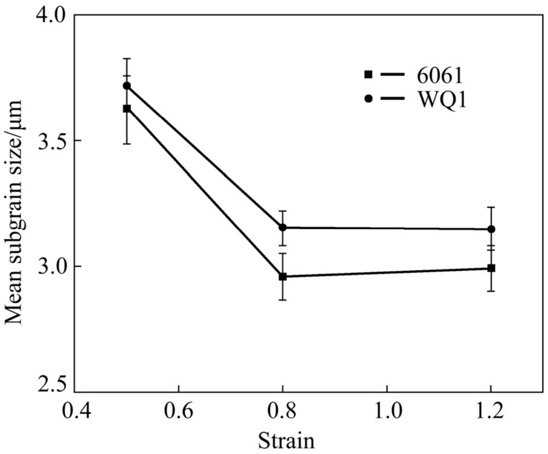

Fig. 6 Evolution of subgrain sizes of 6061 and WQ1 alloys after deformation at 300 °C with strain rate of 0.1 s^{-1} as functions of strain

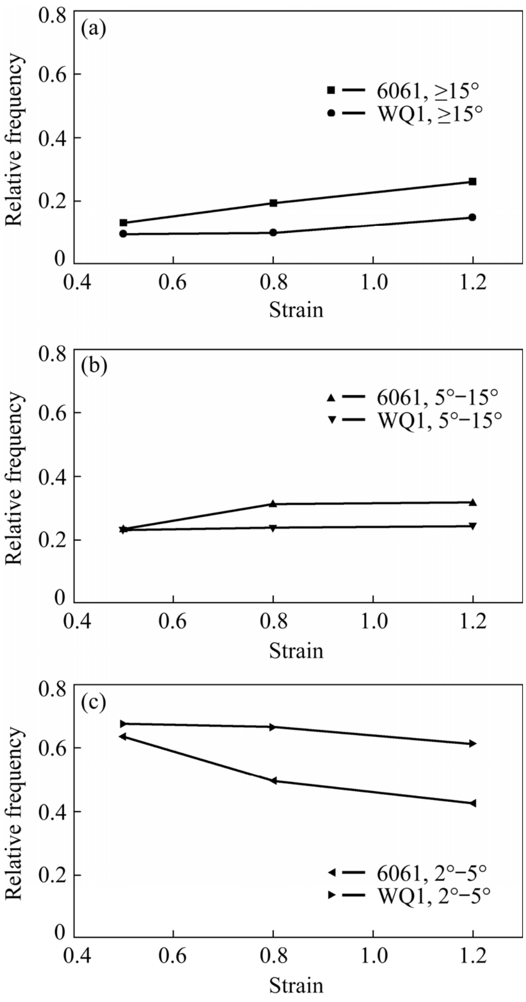

Fig. 7 Frequencies of misorientation for 6061 and WQ1 alloys in regions of ≥15° (a), 5°−15° (b) and 2°−5° (c) as functions of strain

was observed at a strain of 0.8 (Fig. 5(e)). Hence, the substructure rotation in the WQ1 alloy was substantially restrained by the *α* dispersoids, which suppressed the DRV level.

Figure 8 presents the microstructural evolution of the 6061 alloy, which was deformed at various temperatures with a higher strain rate (1 s^{-1}) than that in Fig. 5 to a strain of 1.2, resolved by the EBSD IPF maps. The deformed grain boundaries transformed from laciniate lines to smooth lines with increasing deformation temperature from 300 to 500 °C. Meanwhile, the original grains of the 6061 alloy were separated into several smaller fibrous grains with orientations similar to those of the original grains, as marked by the arrows in Figs. 8(b, c). As shown in Fig. 8(d), the microstructure of the 6061 alloy that was deformed at 300 °C was characterized by massive fully developed subgrain networks across deformed grains. With increasing deformation temperature, the subgrain size obviously increased, and the transformation of LABs to HABs also intensified (red cycles). These phenomena were promoted by increasing the deformation temperature, which activated the self-diffusion of Al and the migration of LABs and HABs. Recrystallization grains were also observed in Figs. 8(d, e, f) (black frames), and their sizes increased with increasing deformation temperature.

Figure 9 shows the microstructural evolution of the WQ1 alloy, which was deformed under the

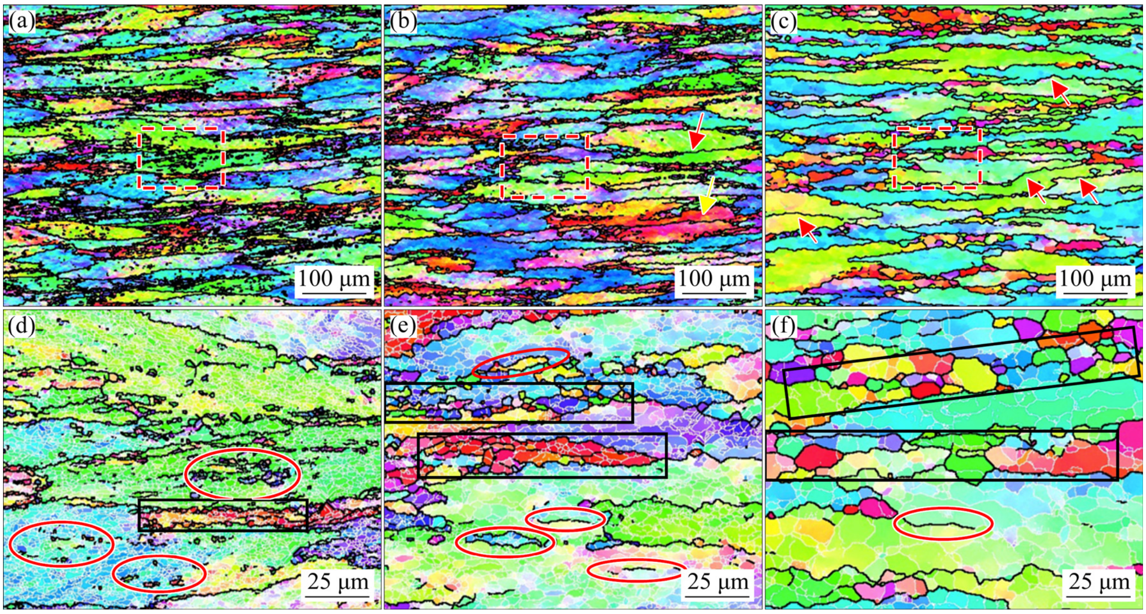

Fig. 8 EBSD IPF images of 6061 alloy deformed at 300 °C (a, d), 400 °C (b, e), 500 °C (c, f), and strain rate of 1 s^{-1} to strain of 1.2

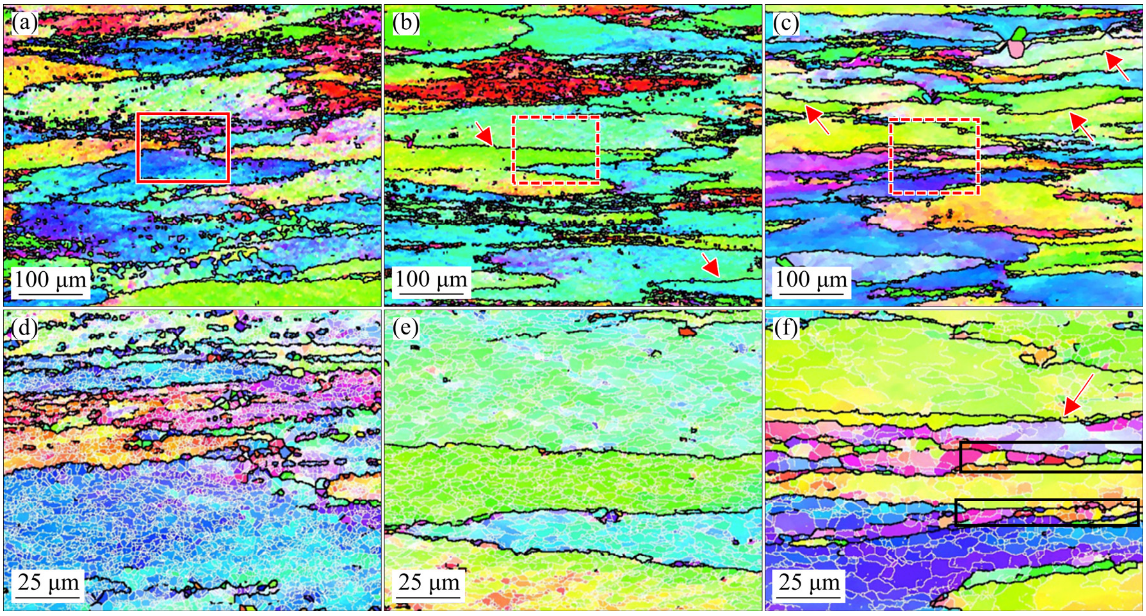

Fig. 9 EBSD IPF images of WQ1 alloy deformed at 300 °C (a, d), 400 °C (b, e), 500 °C (c, f), and strain rate of 1 s^{-1} to strain of 1.2

same conditions as the 6061 alloy (Fig. 8). During the transformation of LABs to HABs, original grains split into fibrous grains with similar orientations, and gDRX was observed in the WQ1 alloy. However, the recrystallized grains in the WQ1 alloy were much smaller and sparser than those in the 6061 alloy, as shown in Fig. 9(f), and DRV remained the predominant mechanism. The evolution of the subgrain size as a function of the deformation temperature is shown in Fig. 10. The subgrain sizes of both alloys increased with increasing temperature. The subgrain sizes of the alloys after deformation at 300 to 400 °C were similar, while the 6061 alloy had a larger subgrain size at 500 °C. This demonstrated that the migration of subgrain boundaries or the combination of subgrains was a main thermal activation process and was accelerated at higher temperature (500 °C). The results show that the Zenner pinning effect caused by α-Al(MnFeCr)Si dispersoids in the WQ1 alloy was more effective at higher temperatures. Hence, the 6061 alloy exhibited a larger subgrain size when the deformation temperature was 500 °C, which was ascribed to the higher deformation temperature and absence of α dispersoids.

Figure 11 shows the misorientation angle distribution in the three regions of the 6061 and WQ1 alloys, which reflect the influence of the deformation conditions on the substructure evolution. Compared with the results in Fig. 7, the substructure frequency was reduced in the region of 2°−5° but increased in the region of 5°−15°. This implies that with increasing deformation temperature, the substructures had a higher frequency of HABs and a lower frequency of LABs, which implies that the subgrains were coarsened and DRX was promoted. LABs were gradually combined or converted into medium-angle boundaries during this process. The subgrain frequencies of both alloys in the region of 2°−5° increased slightly with increasing the deformation

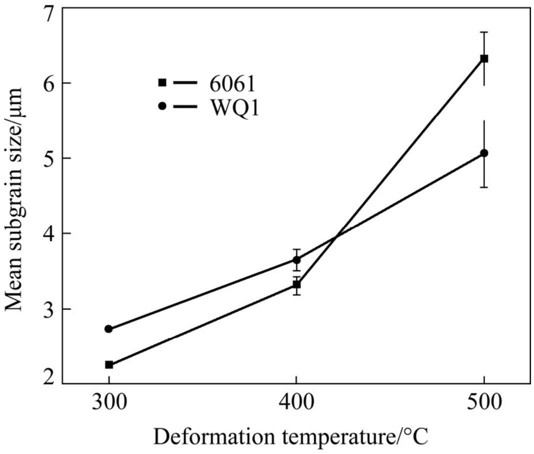

Fig. 10 Evolution of subgrain sizes of 6061 and WQ1 alloys during deformation at strain rate of 1 s^{-1} to strain of 1.2 as functions of deformation temperature

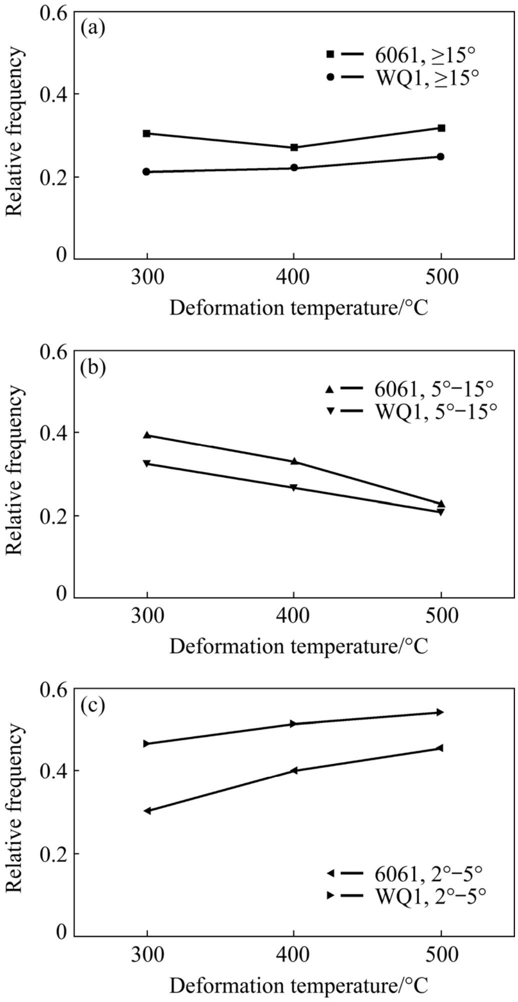

Fig. 11 Frequencies of misorientation for 6061 and WQ1 alloys in regions of ≥15° (a), 5°−15° (b) and 2°−5° (c) as functions of deformation temperature

temperature. In the region of 5°−15°, the subgrain frequencies of both alloys slightly decreased with increasing temperature. The subgrain frequencies of the WQ1 alloy in the region of 2°−5° were always higher than those of the 6061 alloy (Fig. 11(c)) but lower than those in other regions (Figs. 11(a, b)). Due to the *α* dispersoid-restrained DRX in the WQ1 alloy, the frequency of recrystallized grains of the WQ1 alloys was lower than that of the 6061 alloy in the region that corresponded to misorientations of greater than 15°, which is consistent with the results presented in the EBSD maps (Figs. 8 and 9).

To examine the effect of the strain rate on the microstructural evolution, the 6061 and WQ1 alloys were deformed at strain rates of 0.01, 0.1 and 10 s^{-1}, and the corresponding EBSD maps are presented in Fig. 12 and Fig. 13, respectively. For both alloys, the microstructure was characterized by a lower frequency of LABs and a higher frequency of HABs. In the 6061 alloy, which barely contained *α* dispersoids, recrystallized grains were converted from equiaxed grains to rod-like grains and coarsened with decreasing strain rate, as shown in Figs. 12(a, b, c). Recrystallized grains formed internal grains at a lower strain rate, as marked by the black arrows in Figs. 12(d, e).

Although the occurrence of DRX in the WQ1 alloy was not restricted by the presence of *α* dispersoids, the growth of recrystallization grains was obviously restrained, as shown in Fig. 13

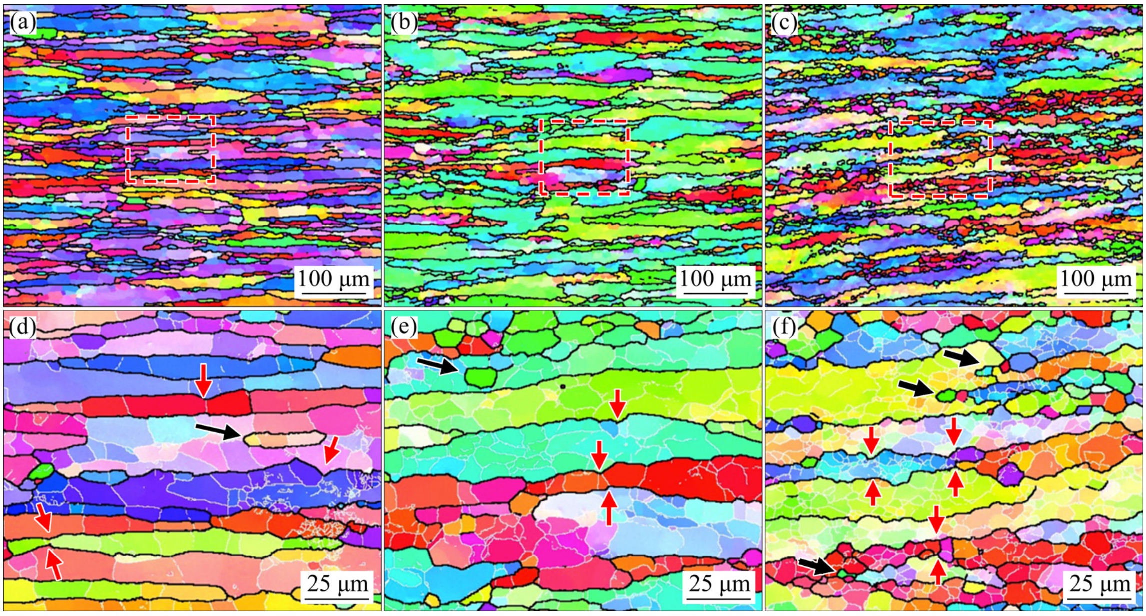

Fig. 12 EBSD IPF images of 6061 alloy deformed at 500 °C with strain rates of 0.01 s^{-1} (a, d), 0.1 s^{-1} (b, e) and 10 s^{-1} (c, f) to strain of 1.2

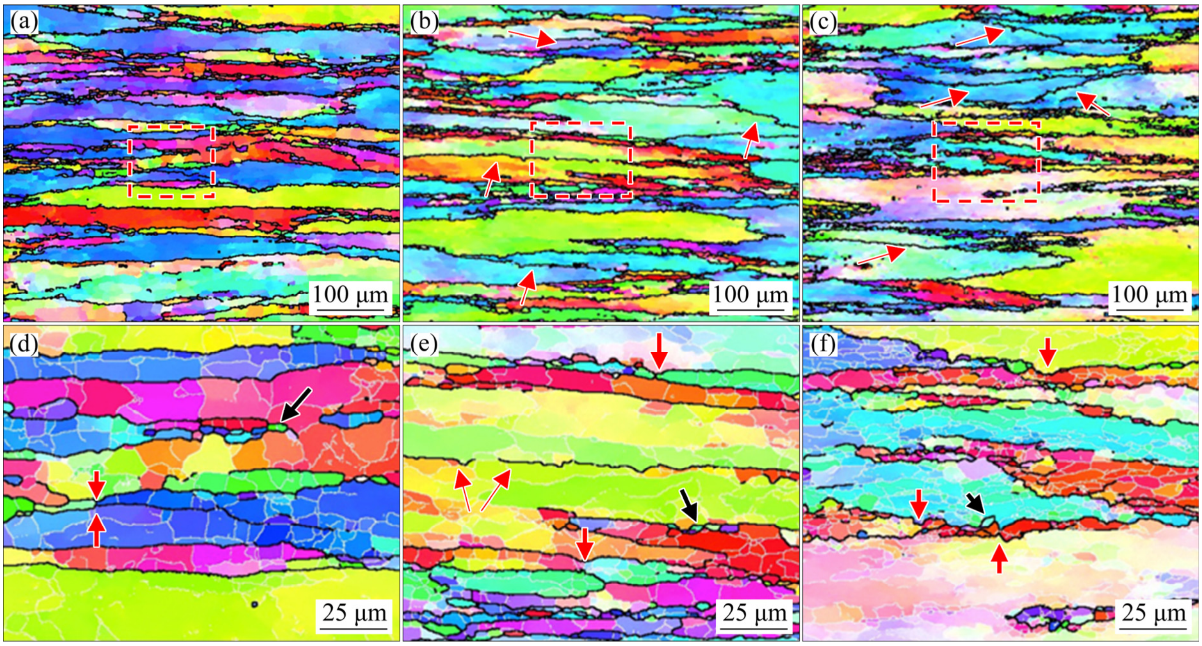

Fig. 13 EBSD IPF images of WQ1 alloy after deformation at 500 °C with strain rates of 0.01 s^{-1} (a, d), 0.1 s^{-1} (b, e) and 10 s^{-1} (c, f) to strain of 1.2

(black arrows). Hence, the microstructure of the deformed WQ1 alloy was characterized by fibrous grains and fine equiaxed grains. The influence of the strain rate on the subgrain size is presented in Fig. 14 for both alloys. The subgrain size dramatically decreased with increasing strain rate. Similar to the result presented in Fig. 10, the WQ1 alloy always had a smaller subgrain size in the presence of α dispersoids. Although the subgrain size of the 6061 alloy was close to that of the WQ1 alloy at a strain rate of 10 s^{-1}, as there was a time limit for DRV, it could not be maintained in the following process (e.g., solution heat treatment).

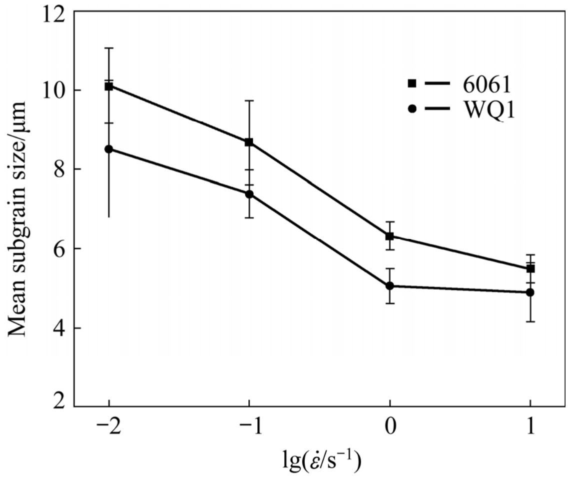

Fig. 14 Evolution of subgrain sizes of 6061 and WQ1 alloys deformed at 500 °C to strain of 1.2 as functions of strain rate

With the deformation temperature rising to 500 °C, the misorientation angle distribution in various regions as functions of the strain rate is shown in Fig. 15, which presents an interesting phenomenon. The misorientation angle of the microstructure was distributed mainly in the regions of 2°−5° and >15° for both alloys. The frequencies of the microstructure in the regions of 2°−5° and ≥15° increased and decreased with increasing strain rate, respectively. Clearly, the growth of recrystallized grains was limited by inadequate time with increasing strain rate, thereby reducing the frequency in the region of ≥15° and increasing the frequency in the region of 2°−5°. However, the frequency of the substructure remained low and was almost constant in the region of 5°−15°, indicating that subgrains with misorientation angles between 5° and 15° converted to HABs, namely, substructures with misorientation angles between 2° and 5° were thermally stable during hot processing and enhanced the final mechanical properties of the alloys. Similar to the results in Figs. 7 and 11, αdispersoids effectively pinned the migration of substructures and subsequently restricted DRV in the WQ1 alloy, especially in the region of 2°−5°.

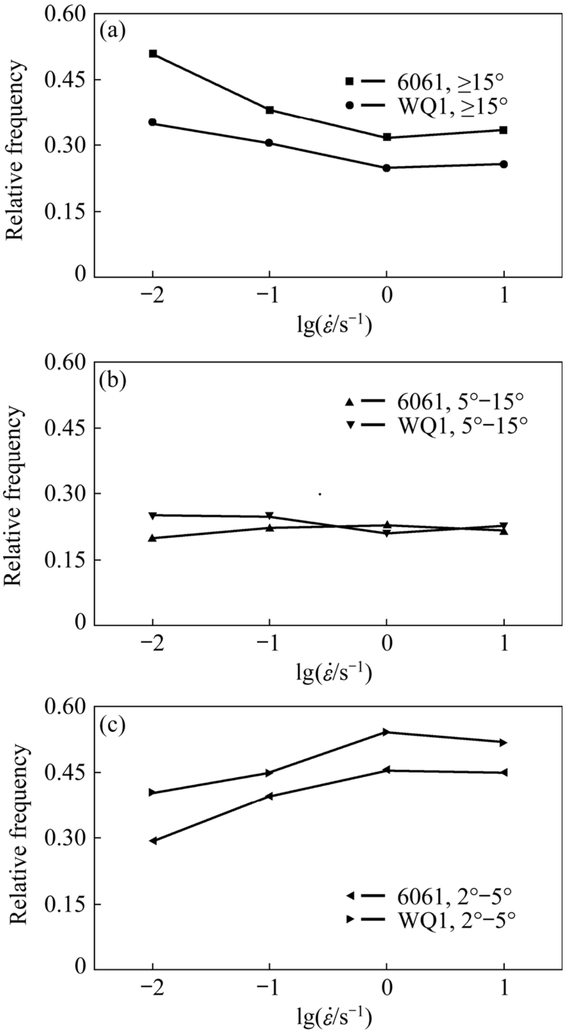

Fig. 15 Frequencies of misorientation for 6061 and WQ1 alloys in regions of ≥15° (a), 5°−15° (b) and 2°−5° (c) as functions of strain rate

4 Discussion

The contents of alloying elements in 6061 and WQ1 are not identical. After homogenization, Mn and Cr were all taken up by precipitation of α-Al(FeMnCr)Si dispersoids, while Mg and Cu were consumed in the form of coarse Mg_2Si and Q precipitates in the 6061 and WQ1 alloys, respectively, during the cooling process. Therefore, limited solute atoms remained in the matrices of both alloys. Due to its relatively large size, the strengthening contribution of precipitated Mg_2Si at ambient temperature could be predicted by the Orowan bypass mechanism. The strengthening contributions of precipitated Mg_2Si to 6061 and WQ1 alloys at room temperature were calculated to be 2.27 and 3.34 MPa, respectively, which became increasingly negligible at elevated deformation temperatures. Therefore, it is reasonable to conclude that the Mn/Cr-containing dispersoids were the main reason for the difference in flow stress between the 6061 and WQ1 alloys.

The microstructural evolution and deformation mechanisms of the 6061 and WQ1 alloys were analyzed by EBSD and studied systematically. The predominant dynamic softening mechanism of the 6061 alloy transformed from DRV to DRV and cDRX with the accumulation of deformation strain and increasing temperature. Meanwhile, DRV was the predominant mechanism in the WQ1 alloy, and only partial gDRX occurred at the original grain boundaries due to the absence of α dispersoids in that area. The DRV levels of both alloys varied due to the transition of LABs to HABs. This process was accompanied by subgrain rotation and combination, which led to the formation of HABs, as shown in Figs. 4 and 5. The combination of newly formed HABs was accelerated by increasing the strain and deformation temperature, which caused fragmentation of the grains, as shown in Figs. 4, 8 and 9. A schematic diagram is presented in Fig. 16 to illustrate how this process promoted fragmentation of the original grains when both alloys were deformed at temperatures exceeding 400 °C. As presented in Fig. 16, the formation process of new HABs within deformed grains occurred by the rotation of adjacent subgrains, which were observed in the 6061 alloy (Figs. 8(c, e, f)), WQ1 alloy (Figs. 9(b, c, f) and Figs. 13(b, c, e)) and were marked by red arrows. The α dispersoids in the WQ1 alloy suppressed the rotation of subgrains and stabilized newly formed HABs, thereby leading to extended lengths, and subsequently segmented the original grains.

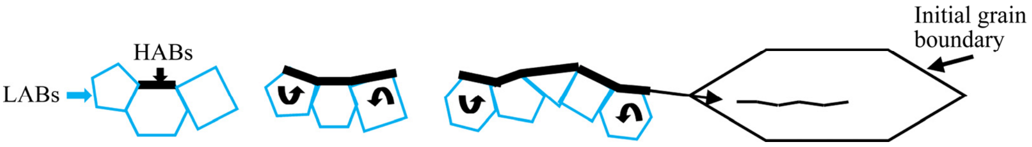

Fig. 16 Schematic diagram of fragmentation of original grains caused by HAB formation during hot deformation

Normally, the occurrence of gDRX depends on the grain size and deformation strain. Although the initial grain size of the WQ1 alloy was larger than that of the 6061 alloy, newly generated HABs (marked by red arrows in Figs. 9(b, c, f) and Figs. 13(b, c, e)) in the interior of the initial grain reduced the distance between HABs, which was conducive to the occurrence of gDRX. In the 6061 alloy, due to the absence of the particle pinning effect, HABs migrated easily and promoted the occurrence of cDRX, thereby resulting in a higher level of DRX. Although *α* dispersoids failed to prevent the occurrence of gDRX in the WQ1 alloy, they obviously restrained the growth of gDRX grains. The occurrence of DRX in both alloys depended on strain, while the growth of recrystallized grains was accelerated by increasing the temperature and decreasing the strain rate. In addition, with the addition of Mn and Cr to the WQ1 alloy, many *α* dispersoids were formed during the homogenization heat treatment, which not only increased the flow stress but also retarded the DRV and restrained the growth of gDRX grains in the deformed microstructure.

Figure 17 presents the interaction between the *α* dispersoids and substructures in WQ1 alloys that were deformed at various temperatures. The microstructure of the WQ1 alloy deformed at 300 °C (Fig. 17(a)) was characterized by a finer subgrain size, which was developed during the DRV process. Additionally, the *α* dispersoids reduced the migration of the subgrain boundaries (as marked by the white arrows in Fig. 17(a)). As the deformation temperature increased to 400 °C (Fig. 17(b)), the subgrains were coarsened and were still accompanied by high-density dislocations. As shown in Fig. 17(c), the dislocation density in the coarsened subgrains dramatically decreased with a further increase in the temperature to 500 °C. Activated by increasing temperature, the substructure mobility was greatly improved, thereby leading to the migration of the subgrain boundaries toward adjacent subgrains with higher storage energies. In addition, HUMPHREYS and HATHERLY [33] concluded that the mobility of the subgrain boundaries dramatically increased with increasing misorientation angle. Hence, the misorientation frequency of the substructure in the region of 5°−15° presented a decreasing tendency with increasing temperature (Fig. 11(b)) but was independent of the deformation strain and strain rate (Figs. 7 and 15). Similarly, the microstructures of both alloys deformed at 500 °C were characterized by subgrains with misorientation angles that were distributed mainly in the region of 2°−5°, which had lower stored energies and mobilities (Fig. 15). Although the pinning effect caused by *α* dispersoids was weakened by increasing temperature, they were still able to retard the migration of subgrain boundaries in the WQ1 alloy with a misorientation angle in the region of 2°−5°.

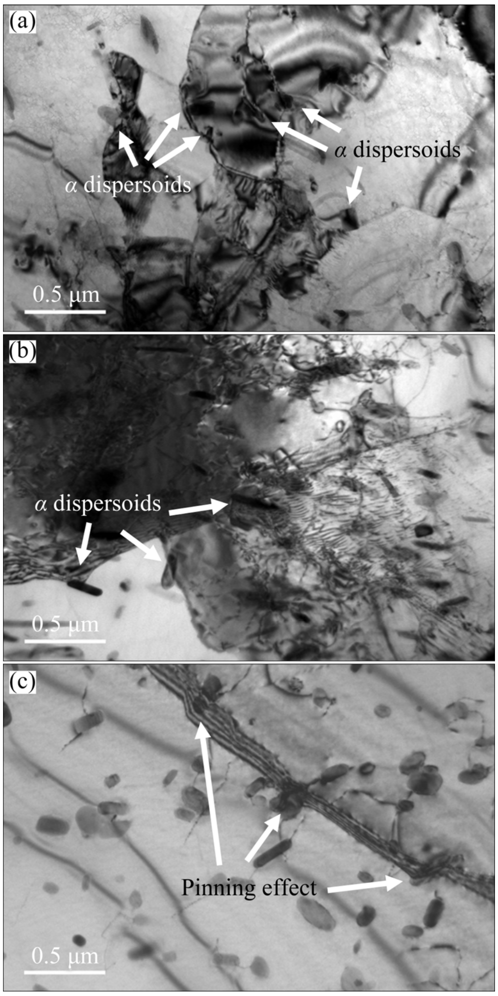

Fig. 17 TEM micrographs of *α* dispersoids interacting with WQ1 alloy substructure at 300 °C (a), 400 °C (b) and 500 °C (c)

As shown in Fig. 18, the mean size of the *α* dispersoids in the WQ1 alloy remained relatively constant with increasing deformation temperature. All hot compression tests were performed at temperatures lower than 500 °C and within 6 min. Hence, the *α* dispersoid size barely changed during the hot compression tests. According to the TEM results, limited precipitation of Mg_2Si occurred during the hot compression process, and the α dispersoids were thermally stable, as discussed above. Therefore, it is concluded that the substructural evolution of both alloys depended on the deformation conditions. According to an empirical equation, the subgrain size (δ) was a function of the Zener−Hollomon parameter (Z), and the relationship between them is expressed as follows [34,35]:

$$\delta^{-1}=A+B\ln Z \tag{1}$$

where A and B are material constants.

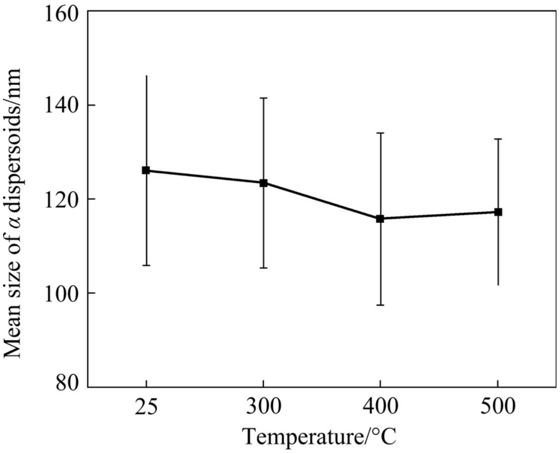

Fig. 18 Mean size of postdeformed α-Al(MnFeCr)Si dispersoids in WQ1 alloy as function of temperature

A generally accepted equation of Z and stress (σ), namely, $Z=A[\sinh(\alpha\sigma)]^n$ [36], can produce better approximations independent of the type of hot deformation. A, α and n are material parameters, which are usually treated as constants. Hence, the subgrain size can be considered a function of the flow stress σ. As illustrated in Fig. 19, for the WQ1 alloy, δ^{-1} and $\ln Z$ exhibit a linear relationship. Therefore, the evolution of the subgrain size is predictable by the analysis of hot compression under varying deformation conditions.

In the analysis of the creep behavior of other particle-strengthening alloys [37], the applied stress is replaced by an effective stress and a threshold stress σ_{th}. The latter represents the influence of the interactions between particles and dislocations. With the threshold stress, the constitutive equation can be rewritten as follows:

$$\dot{\varepsilon}=A\{\sinh[\alpha(\sigma-\sigma_{th})]\}^n\exp[-Q/(RT)] \tag{2}$$

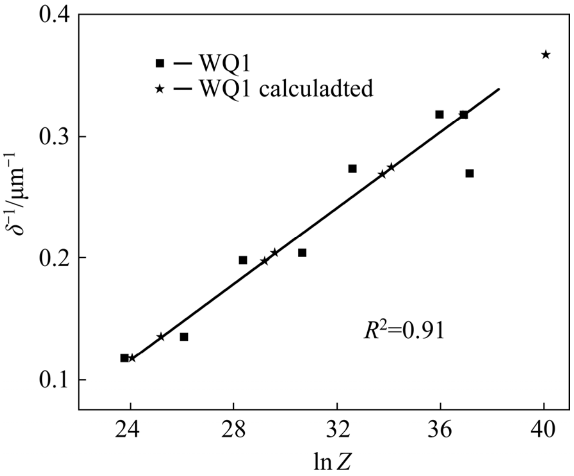

Fig. 19 Subgrain sizes of WQ1 alloys as functions of Z parameter

where Q is the average activation energy, R is the molar gas constant, and T is the thermodynamic temperature.

In Refs. [37,38], σ_{th} was treated as a thermal detachment stress and interpreted as the required stress for detaching dislocations from the particles. Under a low strain rate, σ_{th} was expressed as σ_{Orowan}, and only the contribution from the interaction from one particle with a dislocation was considered. The main distinction between the 6061 and WQ1 alloys is the amount of α-Al(MnFeCr)Si dispersoids in the microstructure. Therefore, the flow stress of the 6061 alloy, which contains few α dispersoids, was treated as the effective stress. Considering the size of the α dispersoids, which is too large for dislocation climbing, the interaction between dislocations and α dispersoids in the WQ1 alloy should be calculated according to the Orowan bypass strengthening mechanism. To theoretically characterize the stress increase from the WQ1 alloy to the 6061 alloy, in consideration of many particles and a constant strain rate, the corresponding Orowan strengthening (σ_{Orowan}) equation was applied and is expressed as [39]

$$\Delta\sigma_{Orowan}=M\frac{0.4Gb}{\pi\lambda}\frac{\ln(2\overline{r}/b)}{\sqrt{1-\upsilon}} \tag{3}$$

where M(=3.06) is the mean orientation factor for aluminum [40], G is the temperature-dependent shear modulus of the matrix alloy, υ is the Poisson's ratio of the aluminum, $\overline{r}=(\sqrt{2/3}\langle r\rangle)$ is the mean radius of the spherical precipitates in a circular cross-section along a random plane, b is the magnitude of the Burgers vector for Al, and λ is the interprecipitate spacing.

According to NEMBACH [41], λ is expressed as

$$\lambda=\{[3\pi/(4f)]^{1/2}-1.64\}r \tag{4}$$

where f(=0.32%) is the volume fraction of the α dispersoids and r=63 nm is the average equivalent radius of the α dispersoids. Considering the temperature dependency of the shear modulus and thermal expansion of Al, the contribution of the α dispersoids at a specified deformation temperature can be calculated based on Eq. (3). The constants used in the calculation are listed in Table 2 [42,43].

Table 2 Constants used in equations

t/°C	G^*/GPa	b^{**}/nm	υ	M
25	25.4	0.286	0.345	3.06
300	21.7	0.288		
400	20.3	0.289		
500	18.9	0.29		

* The temperature dependence of shear modulus is −13.6 MPa/K for Al [42]; ** The thermal expansion coefficient value of Al is 24.7×10^{-6} K^{-1} [43]

The effective stress of the WQ1 alloy, which was the difference between the flow stress and threshold stress, was calculated and compared with the flow stress of the 6061 alloy as a function of the temperature and strain rate, as illustrated in Fig. 20. The calculated effective stress of the WQ1 alloy shows notable agreement with the experimental flow stress of the 6061 alloy under various deformation conditions. This presents an opportunity to predict the effect of α dispersoids with various sizes and volume fractions on the flow stress at various temperatures on microstructural evolution. The Z parameter of the WQ1 alloy can be modified as

$$Z=A'\{\sinh[\alpha(\sigma+\sigma_{\mathrm{th}})]\}^n \tag{5}$$

where A' is the modified material parameter.

The predicted Z value of the WQ1 alloy is presented in Fig. 19, which shows satisfactory agreement with the experimental data. Then, the subgrain sizes of the alloys can be predicted according to Eqs. (1) and (5) at various deformation temperatures and controlled by adjusting the α dispersoid diameter and volume fraction.

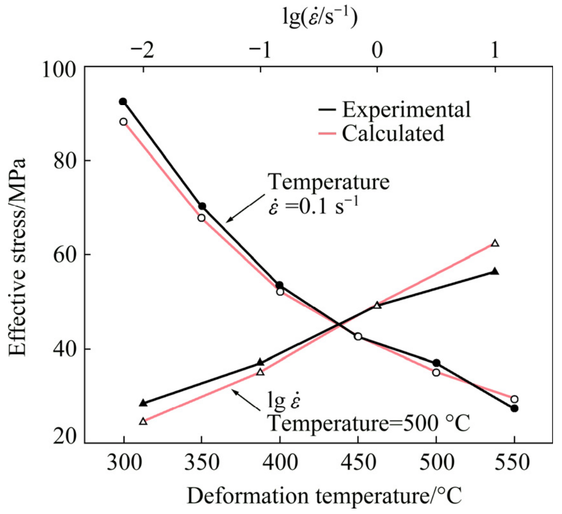

Fig. 20 Experimental and calculated effective stresses of WQ1 alloy as functions of deformation temperature and strain rate

5 Conclusions

(1) The predominant dynamic softening mechanism of the 6061 alloy converted from DRV to DRV and cDRX with increasing temperature, while that of the WQ1 alloy remained DRV. The substructure rotation in the WQ1 alloy was restrained by α dispersoids, which stabilized newly generated HABs in the interior of the initial grain and promoted the occurrence of gDRX.

(2) With increasing deformation temperature and strain rate, α dispersoids could inhibit the mobility of subgrain boundaries with misorientation angles in the region of 2°−5° more effectively than in the region of 5°−15°.

(3) The contributions of α-Al(MnFeCr)Si dispersoids to the flow stress at various temperatures were calculated by a modified Orowan strengthening equation. Based on that, a modification was made to the hyperbolic sin equation to calculate the effect of α dispersoids on the Z parameter. The predicted Z parameter values were consistent with the experimental data and in satisfactory agreement with the subgrain size.

Acknowledgments

The authors are grateful for the financial supports from the National Natural Science Foundation of China (No. U1864209), and Jincheng Science and Technology Plan Project of Shanxi Province, China (No. 201702014).

References

[1] DING Li-peng, JIA Zhi-hong, NIE Jian-feng, WENG Yao-yao, CAO Ling-fei, CHEN Hou-wen, WU Xiao-zhi, LIU Qing. The structural and compositional evolution of precipitates in Al−Mg−Si−Cu alloy [J]. Acta Materialia, 2018, 145: 437−450.

[2] LI Y J, MUGGERUD A M F, OLSEN A, FURU T. Precipitation of partially coherent α-Al(Mn,Fe)Si dispersoids and their strengthening effect in AA 3003 alloy [J]. Acta Materialia, 2012, 60: 1004−1014.

[3] LIU C L, DU Q, PARSON N C, POOLE W J. The interaction between Mn and Fe on the precipitation of Mn/Fe dispersoids in Al−Mg−Si−Mn−Fe alloys [J]. Scripta Materialia, 2018, 152: 59−63.

[4] NAKAI M, ITOH G. The effect of microstructure on mechanical properties of forged 6061 aluminum alloy [J]. Materials transactions, 2014, 55: 114−119.

[5] ZUO Jin-rong, HOU Long-gang, SHI Jin-tao, CUI Hua, ZHUANG Lin-zhong, ZHANG Ji-shan. Effect of deformation induced precipitation on grain refinement and improvement of mechanical properties AA 7055 aluminum alloy [J]. Materials Characterization, 2017, 130: 123−134.

[6] HU Jia-min, TENG Jie, JI Xian-kun, FU Ding-fa, ZHANG Weng-gang, HUI Zhang. Enhanced mechanical properties of an Al−Mg−Si alloy by repetitive continuous extrusion forming process and subsequent aging treatment [J]. Materials Science and Engineering A, 2017, 695: 35−44.

[7] SARKAR J, PRASAD Y V R K, SURAPPA M K. Optimization of hot workability of an Al−Mg−Si alloy using processing maps [J]. Journal of Materials Science, 1995, 30: 2843−2848.

[8] FARKOOSH A R, CHEN X G, PEKGULERYUZ M. Dispersoid strengthening of a high temperature Al−Si−Cu−Mg alloy via Mo addition [J]. Materials Science and Engineering A, 2015, 620: 181−189.

[9] GUEMINI R, BOUBERTAKH A, LORIMER G W. Study of the recrystallization process of AlMgSi alloys containing transition elements [J]. Journal of Alloys and Compounds, 2009, 486: 451−457.

[10] TROEGER L P, STARKE E A Jr. Particle-stimulated nucleation of recrystallization for grain-size control and superplasticity in an Al−Mg−Si−Cu alloy [J]. Materials Science and Engineering A, 2000, 293: 19−29.

[11] KENYON M, ROBSON J, FELLOWES J, LIANG Z Q. Effect of dispersoids on the microstructure evolution in Al−Mg−Si alloys [J]. Advanced Engineering Materials, 2019, 21: 1−7.

[12] HU R, OGURA T, TEZUKA H, SATO T, LIU Q. Dispersoid formation and recrystallization behavior in an Al−Mg−Si−Mn alloy [J]. Journal of Materials Science & Technology, 2010, 26: 237−243.

[13] STROBEL K, SWEET E, EASTON M, NIE J F, COUPER M. Dispersoid phases in 6xxx series aluminium alloys [J]. Materials Science Forum, 2010, 654/655/656: 926−929.

[14] POLETTI C, WÓJCIK T, SOMMITSCH C. Hot deformation of AA6082 containing fine intermetallic particles [J]. Metallurgical and Materials Transactions A, 2013, 44: 1577−1586.

[15] QIAN X M, PARSON N, CHEN X G. Effects of Mn addition and related Mn-containing dispersoids on the hot deformation behavior of 6082 aluminum alloys [J]. Materials Science and Engineering A, 2019, 764: 138253.

[16] GÜZEL A, JÄGER A, PARVIZIAN F, LAMBERS H G, TEKKAYA A E, SVENDSEN B, MAIER H J. A new method for determining dynamic grain structure evolution during hot aluminum extrusion [J]. Journal of Materials Processing Technology, 2012, 212: 323−330.

[17] MEHTONEN S V, PALMIERE E J, MISRA R D K, KARJALAINEN L P, PORTER D A. Dynamic restoration mechanisms in a Ti−Nb stabilized ferritic stainless steel during hot deformation [J]. Materials Science and Engineering A, 2014, 601: 7−19.

[18] McQUEEN H J, IMBERT C A C. Dynamic recrystallization: Plasticity enhancing structural development [J]. Journal of Alloys and Compounds, 2004, 378: 35−43.

[19] KELLY P M. Quantitative electron microscopy [J]. Metals Forum, 1982, 5: 13−23.

[20] SAKAI T, BELYAKOV A, KAIBYSHEV R, MIURA H, JONAS J J. Dynamic and post-dynamic recrystallization under hot, cold and severe plastic deformation conditions [J]. Progress in Materials Science, 2014, 60: 130−207.

[21] ZHANG Cun-sheng, WANG Cui-xue, GUO Ran, ZHAO Guo-qun, CHEN Liang, SUN Wen-chao, WANG Xie-bin. Investigation of dynamic recrystallization and modeling of microstructure evolution of an Al−Mg−Si aluminum alloy during high-temperature deformation [J]. Journal of Alloys and Compounds, 2019, 773: 59−70.

[22] LI Z, QIN J, ZHANG B, NAGAUMI H. Effect of Cr addition on microstructure and mechanical properties at elevated temperature of Al−Mn−Mg−Si alloys [J]. Materials Transactions, 2020, 61: 2095−2100.

[23] CHEN Xiao-xue, ZHAO Guo-qun, ZHAO Xing-ting, WANG Yong-xiao, XU Xiao, ZHANG Cun-sheng. Constitutive modeling and microstructure characterization of 2196 Al−Li alloy in various hot deformation conditions [J]. Journal of Manufacturing Processes, 2020, 59: 326−342.

[24] LI Y S, TAO N R, LU K. Microstructural evolution and nanostructure formation in copper during dynamic plastic deformation at cryogenic temperatures [J]. Acta Materialia, 2008, 56: 230−241.

[25] DHAL A, PANIGRAHI S K, SHUNMUGAM M S. Influence of annealing on stain hardening behaviour and fracture properties of a cryorolled Al 2014 alloy [J]. Materials Science and Engineering A, 2015, 645: 383−392.

[26] KAI Xi-zhou, CHEN Cun, SUN Xia-fei, WANG Chun-mei, ZHAO Yu-tao. Hot deformation behavior and optimization of processing parameters of a typical high-strength Al−Mg−Si alloy [J]. Materials & Design, 2016, 90: 1151−1158.

[27] ZANG Q H, YU H S, LEE Y S, KIM M S, KIM H W. Hot deformation behavior and microstructure evolution of annealed Al−7.9Zn−2.7Mg−2.0Cu (wt.%) alloy [J]. Journal of Alloys and Compounds, 2018, 763: 25−33.

[28] SUN N, PATTERSON B R, SUNI J P, SIMIELLI E A, WEILAND H, ALLARD L F. Microstructural evolution in twin roll cast AA3105 during homogenization [J]. Materials Science and Engineering A, 2006, 416: 232−239.

[29] YANG Qun-ying, DENG Zan-hui, ZHANG Zhi-qing, LIU

Qing, JIA Zhi-hong, HUANG Guang-jie. Effects of strain rate on flow stress behavior and dynamic recrystallization mechanism of Al−Zn−Mg−Cu aluminum alloy during hot deformation [J]. Materials Science and Engineering A, 2016, 662: 204−213.

[30] WANG X, QIN J, NAGAUMI H, WU R, LI Q. The effect of α-Al(MnCr)Si dispersoids on activation energy and workability of Al−Mg−Si−Cu alloys during hot deformation [J]. Advances in Materials Science and Engineering, 2020, 2020: 1−12.

[31] PECH-CANUL M I, KATZ R N, MAKHLOUF M M. Optimum conditions for pressureless infiltration of $\mathrm{SiC_p}$ preforms by aluminum alloys [J]. Journal of Materials Processing Technology, 2000, 108: 68−77.

[32] DONG Qi-peng, CHEN Xia-ming, XIA Jun, LI Xin-zhong, ZHANG Bo, NAGAUMI H. Floating grain characterization and its effects on centerline segregation of direct-chill cast Al−Mg−Si alloy billets [J]. Materials Transactions, 2020, 61: 2386–2392.

[33] HUMPHREYS F J, HATHERLY M. Recrystallization and related annealing phenomena [M]. 2nd ed. Amsterdam: Elsevier, 2004: 333−378.

[34] MCQUEEN H J, EVANGELISTA E, BOWLES J, CRAWFORD G. Hot deformation and dynamic recrystallization of Al−5Mg−0.8Mn alloy [J]. Metal Science, 1984, 18: 395−402.

[35] DUAN X J, SHEPPARD T. Simulation and control of microstructure evolution during hot extrusion of hard aluminium alloys [J]. Materials Science and Engineering A, 2003, 351: 282−292.

[36] HARADA Y, DUNAND D C. Microstructure of $\mathrm{Al_3Sc}$ with ternary rare-earth additions [J]. Intermetallics, 2009, 17: 17−24.

[37] SPIGARELLI S, MEHTEDI M E, CICCARELLI D, REGEV M. Effect of grain size on high temperature deformation of AZ31 alloy [J]. Materials Science and Engineering A, 2011, 528: 6919−6926.

[38] SPIGARELLI S, EVANGELISTA E, MCQUEEN H J. Study of hot workability of a heat treated AA6082 aluminum alloy [J]. Scripta Materialia, 2003, 49: 179−183.

[39] CHAWLA K, MEYERS M. Mechanical metallurgy: Principles and applications [M]. NJ: Prentice-Hall, 1984.

[40] QIN J, ZHANG Z, CHEN X G. Mechanical properties and thermal stability of hot-rolled Al−15%$\mathrm{B_4C}$ composite sheets containing Sc and Zr at elevated temperature [J]. Journal of Composite Materials, 2017, 51: 2643−2653.

[41] NEMBACH E. Particle strengthening of metals and alloys [M]. New York: Wiley-VCH, 1996.

[42] FROST M, ASHBY H J. Deformation mechanism maps: The plasticity and creep of metals and ceramics [M]. Oxford, UK: Pergamon Press, 1982.

[43] TOULOUKIAN Y S. Thermophysical properties of high temperature solid materials [M]. New York: The Macmillan Company, 1967.

定量分析 α-Al(MnFeCr)Si 弥散相对 Al−Mg−Si 合金热变形和显微组织演变的影响

Hiromi NAGAUMI [1,2]，秦 简 [1,2]，于承斌 [1,2]，王孝国 [1,3]，王林生 [4]

1. 苏州大学 高性能金属结构材料研究院，苏州 215021；
2. 苏州大学 沙钢钢铁学院，苏州 215021；
3. 山西农业大学 农业工程学院，太谷 030801；
4. 澳美铝业，佛山 528000

摘 要：通过在 300~500 °C 及不同应变速率条件下的热压缩试验研究 AA6061 和含锰 Al−Mg−Si−Cu 合金的显微组织演变规律。与 AA6061 合金相比，含锰 Al−Mg−Si−Cu 合金中大量的 α-Al(MnFeCr)Si 弥散相有效提高了所有变形条件下合金的流变应力。通过电子背散射衍射测量研究变形参数对显微组织演变的影响。两种合金的主要软化机制为动态恢复。含锰合金中 α 弥散相的存在有效地细化了取向差为 2°~5°的亚结构，从而抑制动态恢复。为了预测不同变形条件下的亚晶粒尺寸，通过修正的 Orowan 方程计算 α 弥散相的加入导致的阈值应力，并将其纳入传统的本构方程中。采用修正的本构方程计算的亚晶尺寸与实验数据显示出良好的一致性。

关键词：Al−Mg−Si 合金；热变形；α-Al(MnFeCr)Si 弥散相；亚结构；动态软化；阈值应力；*Z* 参数

(Edited by Wei-ping CHEN)